Review of Scientific Instruments ARTICLE scitation.org/journal/rsi

Compact sample environment for *in situ* X-ray scattering during spin-coating

Cite as: Rev. Sci. Instrum. 94, 063901 (2023); doi: 10.1063/5.0149613
Submitted: 7 March 2023 • Accepted: 14 May 2023 •
Published Online: 2 June 2023

Ekaterina Kneschaurek,[1,a] Alexander Hinderhofer,[1,b] Bernd Hofferberth,[1] Niels Scheffczyk,[1] Linus Pithan,[1] Paul Zimmermann,[1] Lena Merten,[1] Florian Bertram,[2] and Frank Schreiber[1,c]

AFFILIATIONS

[1] Institute of Applied Physics, University of Tübingen, 72076 Tübingen, Germany
[2] Deutsches Elektronen-Synchrotron DESY, Notkestr. 85, 22607 Hamburg, Germany

[a] **Author to whom correspondence should be addressed:** ekaterina.kneschaurek@uni-tuebingen.de
[b] alexander.hinderhofer@uni-tuebingen.de
[c] frank.schreiber@uni-tuebingen.de

ABSTRACT

We demonstrate a compact sample environment for the *in situ* study of crystallization kinetics of thin films on synchrotron beamlines, featuring atmospheric control, automated deposition, spin-coating, and annealing stages. The setup is suitable for studying thin film growth in real time using grazing-incidence X-ray diffraction techniques. Humidity and oxygen levels are being detected by sensors. The spinning stage exhibits low vertical oscillation amplitude (~3 μm at speeds up to 10 000 rpm) and can optionally be employed for antisolvent application or gas quenching to investigate the impact of these techniques, which are often used to assist thin film growth. Differential reflectance spectroscopy is implemented in the spin-coater environment for inspecting thin film thickness and optical properties. The infrared radiation-based annealing system consists of a halogen lamp and a holder with an adjustable lamp-to-sample distance, while the sample surface temperature is monitored by a pyrometer. All features of the sample environment can be controlled remotely by the control software at synchrotron beamlines. In order to test and demonstrate the performance, the crystallization pathway of the antisolvent-assisted $MAPbI_3$ (MA = methylammonium) perovskite thin film during the spinning and annealing stages is monitored and discussed.

I. INTRODUCTION

Real time *in situ* X-ray and neutron scattering experiments are one of the most common techniques for material characterization.[1–6] The high brilliance of modern synchrotron radiation sources allows direct observation of thin film growth *in situ* with high temporal and spatial resolution.[7,8] In particular, grazing incidence X-ray scattering methods reveal microstructure features including crystal structure, polymorphism, grain size and mosaicity, preferential orientation, in-plane texture, and grain boundaries.[9,10] In order to control the full growth procedure of different materials at synchrotron facilities, numerous sample environments with specific deposition conditions have been developed in the past.[11–16]

Organic and hybrid thin films play a key role in modern electronics and optoelectronics.[17,18] Extensive study of their structural and optical properties leads to a better understanding of the mechanism of thin film growth during thin film preparation.[19–21] Solution-based procedures are widely used for organic thin film fabrication, including spin-coating, spray-coating, dip-coating, blade-coating, and roll-coating.[22,23] These methods are established for depositing thin films with good homogeneity and low surface roughness. Spin-coating is one of the vital routes for laboratory-scale sample fabrication. It is a rapid and simple method for providing optimal thin film morphology and thickness ranging from a few nanometers to a few micrometers.[24] Multiple chambers for X-ray scattering-based thin film characterization during spin-coating were previously developed.[25–28] A wide range of materials can be studied during spin-coating, for example, polymer thin films,[4,29,30] small-molecule organic semiconductors,[31,32] coupled organic-inorganic nanostructures (COINs),[33,34] and perovskite thin films.[35–42]

Our setup meets the challenge of minimum wobble at high rotation speeds, which is crucial for grazing incidence wide-angle X-ray scattering (GIWAXS), and also has complementary sample manipulation and characterization tools. A detailed description

of the remotely operated systems is presented in this article. The designed chamber is dedicated for GIWAXS measurements at beamline P08[43] at PETRA III/DESY and fits on any beamline with a hexapod. We test the performance of our compact sample environment by studying antisolvent-assisted $MAPbI_3$ perovskite thin film crystallization during spin-coating in real-time by *in situ* GIWAXS.

II. CHAMBER DESIGN AND CONCEPT

The grazing incidence geometry (Fig. 1) is characterized by a low angle of incidence (α = 0°–1°), which is defined as the angle between the incoming X-ray beam and the sample surface. The scattering angle 2θ is measured from the direction of the incoming beam to the direction of the observation of the scattered beam.

The general concept of the sample environment is shown in Fig. 2(a). The main part of the experimental setup consists of a cuboid housing (225 mm (vertical) × 210 mm × 210 mm) made of stainless steel with Kapton® windows for the incident and scattered X rays. The size of the window for the scattered X rays is 120 mm (horizontal) × 90 mm (vertical) to cover the in-plane direction with a maximum angle of 27.5° and the out-of-plane direction with a maximum angle of 38°. The deposited material lands on the windows during the spin-coating procedure. With the most tested setup (40 μL, <5000 rpm), all droplets hit the windows below the X-ray beam path. During extensive use of the spin-coating chamber, it is recommended to change the windows frequently to avoid cross contamination between different sample compositions.

Since the regular beam sizes are typically below 0.1 mm, they bring very strict requirements for the vertical and angular displacements of the sample table during spin-coating. Therefore, the spinning system was optimized to have low deflection along the axial direction. Some details on its development are discussed in Sec. II A. The spin-coating procedure requires a remotely controlled liquid delivery system, which is provided by a micropipette mechanism. Antisolvent-assisted growth[44–46] and gas-quenching[47–49] are two common procedures that can be applied during spinning, and both of them are supported in our compact environment. The atmosphere monitoring system consists of humidity and oxygen sensors placed at the height of the sample for precise measurements. The annealing system consists of a halogen infrared (IR) lamp fixed to a mechanism for adjusting the distance to the sample and a pyrometer pointing at the sample surface to monitor/record the temperature. Visual control of the thin film deposition steps is performed by a camera (Pi®RASP CAM HQ CMOS) directed at the sample surface area, which gives immediate feedback regarding thin film solidification and color change during spinning and annealing procedures. Film thickness and estimation of optical properties are performed by Differential Reflectance Spectroscopy (DRS) fixed on the top lid of the chamber with its beam focused in the center of the sample.

Experiments at synchrotron facilities ultimately require remote control of the devices with their software being integrated into the beamline infrastructure. This feature allows one to control all devices related to the sample environment through the beamline control system to automatically start spinning, antisolvent application, or gas quenching, and subsequently anneal the sample to follow the exact production procedure. A technical drawing of the designed chamber and a photo of the spin-coating environment in operation at beamline P08[43] at DESY are shown in Figs. 2(b) and 2(c), respectively.

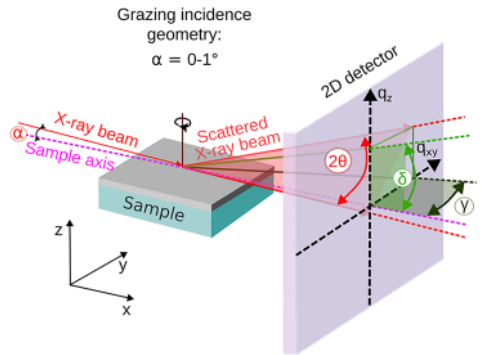

FIG. 1. Geometry of an X-ray scattering experiment. The (longitudinal) *Sample axis* is the projection of the incoming X ray on the sample surface. The X-ray incident angle (α) and in-plane exit angle (γ) are measured from the *Sample axis*. The X-ray out-of-plane exit angle (δ) is measured from the sample surface. The scattering angle 2θ is measured between the incident beam and the scattered beam.[4] Grazing incidence geometry corresponds to an angle of incidence of α = 0°–1°.

A. Spin-coating system

The grazing incidence geometry brings certain limitations to the vertical (1) and angular (2) displacements of the sample table during rotation: (1) originates from the magnetic field of the motor, is reproducible, and can be corrected prior to spinning, while (2) comes from the motor rod/sample table tilt and their vibration. The optimization of (2) for the spinning system was performed by choosing a stable in-runner motor, selecting the best geometry of the sample table, and testing out screw configurations for fixing the table on the motor rod: three M3 screws with an angle of 120° between them were used. Since the screw tightening induces some tilt, a counterforce has to be applied by pressing the sample table while fixing each screw to keep the table surface flat.

The spinning system consists of a motor DB42S02 from Nanotec fastened inside a housing and a sample table (45 mm in diameter) fixed by three M3 screws on the rotating rod. Samples up to a size of 17 × 17 mm^2 can be attached with heat-resistant sticky tape or silver paste. The static and periodic vertical displacements of the sample table were measured by a capacitive sensor D-510.101 PISeca from Physik Instrumente placed in proximity to the sample table. The change in capacitance is transformed into the change in sensor-to-sample table distance by the E-852 PISeca signal evaluation electronics. Two types of vertical sample table displacement during rotation were measured: the static part in Fig. 3(a) and the periodic part in Fig. 3(b). Once the spinning starts, the sample table is lifted by the magnetic force in the vertical direction. This value is dependent on the rotation frequency and goes up to ~19.5 μm. The periodic displacement amplitude, which originates from sample table tilt and vibration, was measured at the edge of the sample table and in the center and is, on average, 5.5 and 2.5 μm, respectively. The increase in the periodic displacement above 8000 rpm takes place because of the motor resonance. Since the vertical size of

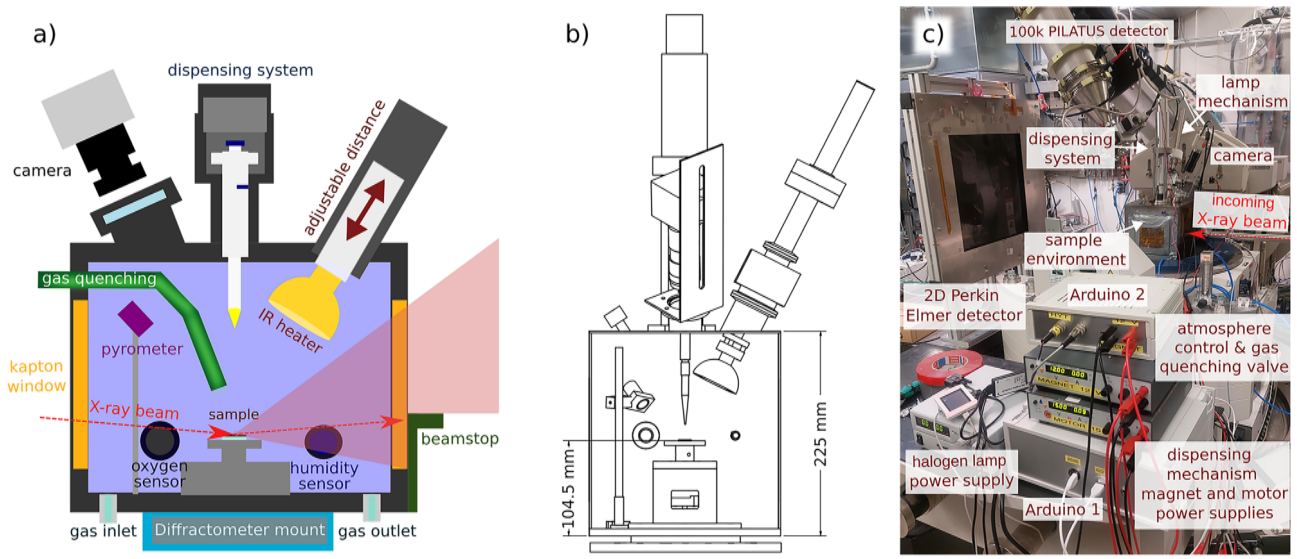

FIG. 2. Spin-coating chamber for *in situ* GIWAXS measurements: (a) general concept including all the major parts; (b) technical drawing of the chamber; (c) photo of the chamber in operation at beamline P08 at PETRA III (DESY).

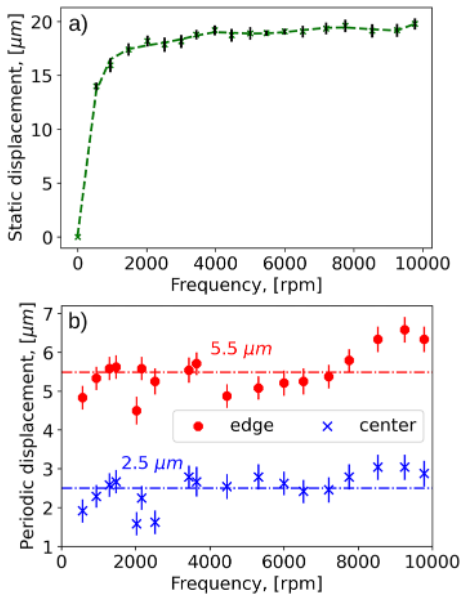

FIG. 3. The sample table vertical displacement amplitude: (a) static part, which remains constant (19.5 μm) from 4000 rpm up to 10 000 rpm, and (b) periodic part at the edge and center during each rotation of the sample table.

the incoming X-ray beam is on the order of ~100 μm, this wobbling will only slightly change the intensity due to the change in the incident angle. The average angular displacement of the sample table of the spin-coater at frequencies up to 10.000 rpm is ~0.01○, which is at least one order of magnitude smaller than typical angles of incidence for surface-sensitive GIWAXS.

B. Dispensing system

Spin-coating is a solution-based technique; therefore, liquid delivery is a crucial step of the procedure. Once the substrate is fixed on the sample table and the incoming X-ray beam is aligned, the precursor solution has to be deposited. As a dispensing system, we use a remotely controlled magnet-based micropipette pressing mechanism that provides sub-100 ms delivery speed. Small volumes of precursor solutions (40–60 μL) are reliably delivered by 100 or 200 μL micropipettes without spontaneous dropping.

In order to assist thin film crystallization, antisolvent-assisted growth and gas quenching (Fig. 4 and inset, respectively) were implemented into our compact environment. Big volumes of antisolvent (150–250 μL) can be reliably delivered by a 1000 μL volume micropipette.[50] Gas-assisted thin film crystallization is supported by a high-density polyethylene tube in a brass tube guide directed at the sample surface and a magnetic gas valve MHJ10-S-2,5-QS-6-HF switched with an I/O output.

C. Atmosphere control system

Some thin films, such as perovskites, are typically grown inside a glove box flushed with nitrogen with low oxygen and humidity values. The presence of an inert atmosphere inside the compact sample environment is provided by the inlets on the bottom and top of the chamber and is controlled by a humidity sensor HYT939 from B + B Sensors and an oxygen sensor SGX-VOX from SGX Sensortech located at the sample height for precise measurements. The sensors are vertically oriented and shielded by foil. No small droplets were

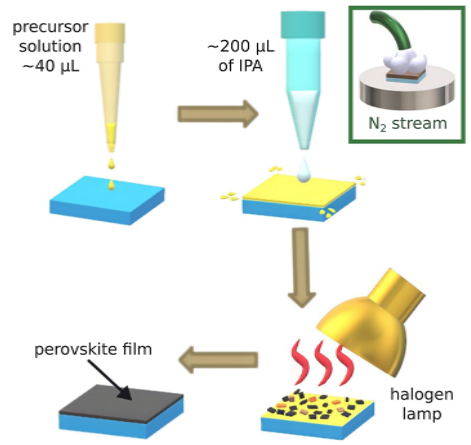

FIG. 4. Step-by-step spin-coating procedure with antisolvent application or gas quenching (shown in the inset) and subsequent annealing.

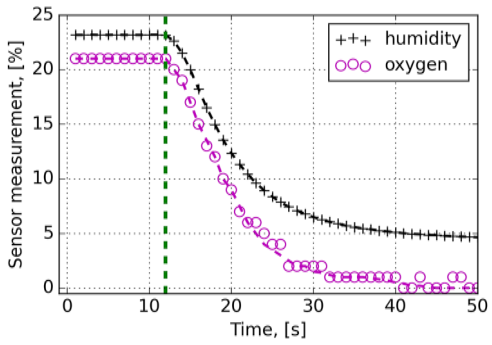

FIG. 5. Humidity (black crosses) and oxygen (magenta circles) percentages measured with sensors placed inside the chamber on the sample height. The green dashed line shows when 2 bar nitrogen was switched on.

found on the surfaces of the humidity and oxygen sensors. Typical humidity and oxygen percentage values after switching on the 2 bar nitrogen flow can be found in Fig. 5, which shows the drop of humidity from 23% to 5% and oxygen from 21% to 0% within ~30 s of nitrogen flushing. When some of the deposited material in a vapor state adsorbs on the sensor surface, it may influence the readouts of the sensors.

D. Annealing system

The spin-coating process frequently requires subsequent annealing. For this purpose, an IR heater is installed. The heating system consists of a halogen lamp 64 635 HLX from OSRAM with a golden reflector having a maximum power of 150 W and a color temperature of 3200 K attached to a magnet-based custom-built lamp mechanism with adjustable lamp-to-sample distance and connected to a VOLTCRAFT PPS-16005 power supply (1–36 V/DC, 0–10 A).

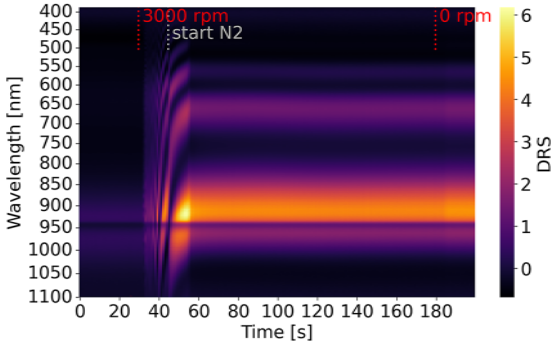

FIG. 6. DRS measurement during the spin coating step. The dotted lines show the start and stop of the spin process and gas flow. At 30 s, the motor starts spinning up to 3000 rpm. 45 s into the scan, a nitrogen flow is directed at the sample.

The sample annealing procedure strongly depends on the substrate material: ITO coating, for example, absorbs IR light[51] and thus serves as a heat reservoir, annealing the precursor solution from the bottom and complementing the direct heating by the lamp from the top. Then, for the lamp-to-sample distance of 40 mm and lamp power of 150 W, an ITO-coated glass substrate heats up to 100 °C in 30 s and approaches 200 °C in 180 s. During the experiment, the temperature of the sample surface is measured by a pyrometer CT-SF15 from Micro-Epsilon with a small angle of view (15°) and a controller operated by an RS232 interface.

E. Differential reflectance spectroscopy

For the *in situ* investigation of the optical properties of perovskite thin films, DRS is included in the chamber. During the experiment, light from a white light source (DH-2000 deuterium–tungsten halogen lamp) goes through the RP22 200 μm 0.22NA 250–1200 nm optical fiber and is directed onto the sample by an achromatic lens (Edmund Optics, focal length = 8 cm). The reflected light is detected by a charge-coupled device (CCD,

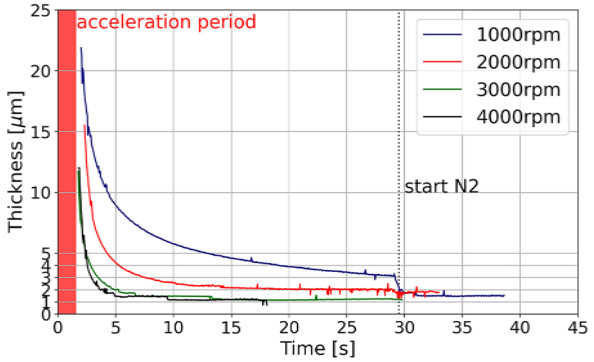

FIG. 7. Thickness calculated from DRS data during the spin coating process. The motor was started at 0 s but takes 2–3 s to get to the desired rotation speed. Nitrogen flow is started shortly before 30 s.

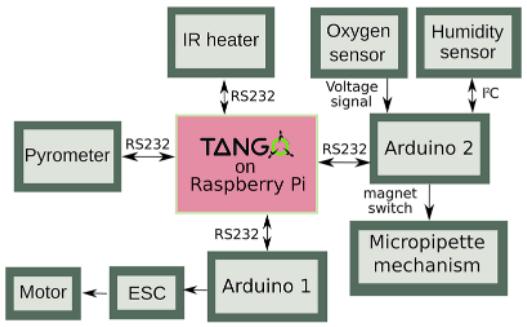

FIG. 8. Communication diagram of the spin-coater devices controlled via TANGO installed on a Raspberry Pi. The IR heater and pyrometer are directly controlled by RS232 serial communication; the ESC running the motor is controlled via Arduino 1; all other devices are controlled by Arduino 2. The humidity sensor uses the I^2C protocol, the oxygen sensor gives a voltage signal proportional to oxygen level, and the micropipette mechanism is triggered by a 12 V signal.

USB2000+, Ocean Optics). The detector has an energy range of E = 387–1100 nm and an optical resolution of $\Delta\lambda$ = 0.1 nm. It is possible to record up to 1000 spectra every second. As a demonstration, we show a DRS measurement of a typical $MAPbI_3$ thin film growth during the gas quenching-assisted spin-coating process in Fig. 6. By analyzing thin film interference, measured by DRS, we can calculate the film thickness during spincoating (Fig. 7). The measurements showed the trajectory expected from the literature.[52] With this method, the thickness could be measured in a range of 1 to 22 μm. The upper limit is due to noise, and the lower limit is due to the limited spectral range. Depending on the sample conditions, the DRS signal can also be used to model the absorption coefficient of the sample during preparation. With precise knowledge of the complex refractive index of the spin-coated material, in principle, also smaller thicknesses can be extracted by modeling and fitting the data with, e.g., the transfer-matrix method.

F. Software infrastructure

The spin-coater setup consists of different devices, and its communication diagram is shown in Fig. 8. The central part represents TANGO device servers running on a Raspberry Pi with all devices connected, where TANGO is a free open source device-oriented control toolkit. This feature makes our spin-coater software compatible with synchrotron facilities using TANGO and allows the device to be controlled from the main beamline control computer and from within the beamline control software (e.g., Spock/Sardana at P08 of PETRA III/DESY, Hamburg). The spin-coating motor is controlled by an Arduino via an electronic speed controller (ESC). The micropipette mechanism with the magnetic switch, humidity, and oxygen sensors are controlled by a second Arduino. The dispensing mechanism is triggered by switching off the electromagnet; the humidity sensor HYT 939 from Conrad Electronic is communicating via I^2C protocol, whereas the oxygen sensor generates an output voltage signal transformed into an oxygen level in %. The annealing system consists of a pyrometer and a lamp power supply, both of which use RS232 communication.

The increased amount of scattered data has led to the application of machine learning methods for its analysis.[53–56] Since the *in situ* GIWAXS experiments generate a large amount of data that must be analyzed, the designed chamber can be used in combination with deep learning-based feature detection,[57] which is capable of identifying crystal structures from Bragg peaks on the fly during thin film crystallization. It allows one to adjust and optimize annealing parameters in the event of incomplete conversion of the intermediate phases into the expected crystal structure. Apart from that, the preliminary analysis already performed during data acquisition allows one to classify the resulting samples and makes post-processing simpler.

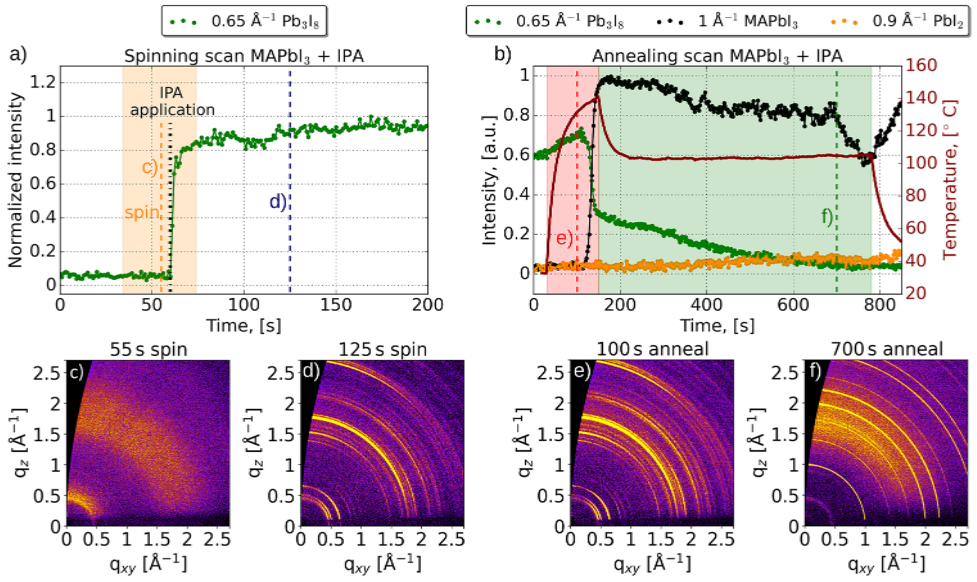

FIG. 9. Scattering intensity evolution of the structures extracted from *in situ* GIWAXS during (a) antisolvent-assisted spin-coating and (b) annealing steps of $MAPbI_3$ perovskite thin film fabrication. The dark red line in (b) shows the temperature of the glass substrate measured with a thermocouple at the same annealing parameters: 120 s at 150 W (red region) and 630 s at 85 W (green region). The vertical lines in the graphs correspond to the images (c)–(f). Exemplary GIWAXS scans: (c) before and (d) after IPA application; (e) intermediate phase, which is fully converted into (f) perovskite thin film with a tiny fraction of PbI_2 after annealing.

III. DEMONSTRATION OF THE PERFORMANCE

As a demonstration, we show typical $MAPbI_3$ thin film growth on a 1 mm thick 10×10 mm^2 bare glass substrate. The experiment was conducted at the P08 beamline[43] at PETRA III/DESY. Precursor solution was prepared by dissolving 1.4 M MAI and PbI_2 in 4:1 DMF:DMSO solvent mixture, where DMF is dimethylformamide, (CH3)NC(O)H and DMSO is dimethyl sulfoxide, $(CH_3)_2SO$. The sample fabrication procedure was as follows: 40 μl of perovskite precursor solution was applied onto the argon plasma-cleaned substrate and spin-coated for 10 s at 1000 rpm and 30 s at 4000 rpm. 200 μl of isopropanol (IPA) antisolvent was applied 10 s before the spinning was finished. *In situ* GIWAXS patterns were acquired using 18 keV X rays (λ = 0.69 Å) with a beam size of 500 μm (horizontal) × 100 μm (vertical) at an angle of incidence of 0.5° at 0.1 s intervals by a 2D PerkinElmer detector (XRD 1621 CN3 EHS, 2048 × 2048 pixel) located at a distance L = 809 mm from the sample. Figure 9 shows the peak intensity evolution of the structures growing in the sample during (a) spin-coating and (b) annealing procedures in the following sequence: Fig. 9(c) shows the start of spinning, indicating structural density increase with broad features around 0.6 Å^{-1} corresponding to scattering from a nearly amorphous precursor phase and 2 Å^{-1} related to the bare glass substrate signal. The antisolvent drop at 60 s induces the removal of DMF and DMSO solvents [Fig. 9(d)], resulting in a fast intensity increase of an intermediate phase, namely, a $(MA)_2Pb_3I_8 \cdot 2DMSO$ solvent complex[58] (marked as Pb_3I_8). Its intensity was slowly increasing even after spin-coating, indicating ongoing crystallization.Please add important details on chemical composition: Precursor solution was prepared by dissolving 1.4 M MAI and PbI_2 in 4:1 DMF:DMSO solvent mixture, where DMF is dimethylformamide, (CH3)NC(O)H and DMSO is dimethyl sulfoxide, $(CH_3)_2SO$.

The subsequent annealing procedure is shown in Fig. 9(b). The heater-to-sample distance was 40 mm, and the lamp power was 150 W for 120 s, followed by heating at 85 W for 630 s. The annealing initiates solvent evaporation, which results in increased scattering intensity of diffraction rings located at 0.45, 0.51, and 0.65 Å^{-1} corresponding to the Pb_3I_8 complex[58] [Fig. 9(e)], taking place until 120 s. Then, the intermediate phase is converted in two steps into the $MAPbI_3$ perovskite phase with an intense diffraction ring at 1 Å^{-1}. The quick conversion has presumably started near the surface, whereas, due to the annealing nature of an IR heater, the bulk was crystallizing slower. After the full intermediate-to-cubic conversion, a small amount of PbI_2 with a peak at 0.9 Å^{-1} was observed [Fig. 9(f)]. Our compact sample environment allowed us to follow the complete process of thin film crystallization and highlight essential steps by observing thin films with *in situ* GIWAXS.

IV. CONCLUSION

We were able to meet the requirements of the *in situ* synchrotron experiments by designing a compact spin-coating environment with a small wobbling amplitude (~3 μm at frequencies up to 10 000 rpm) and remotely controlled systems. The present article provides precise technical details of all components used in the chamber; all of them are commercially available. The systems provide appropriate conditions for the process of thin film growth. Solution delivery, antisolvent application, or gas quenching are designed to support the spinning procedure. The annealing system consists of an IR heater with an adjustable lamp-to-sample distance and a pyrometer targeted at the sample surface. The chamber is connected to the local inert gas supply lines, and the atmosphere is monitored in real-time by humidity and oxygen sensors placed at the sample height for precise measurements. For the inspection of optical properties and film thickness, DRS measurements can be performed. The software for controlling different systems has a TANGO layer and is compatible with beamline infrastructure. Feature detection developed for tracking thin film crystallization via deep-learning systems and identifying the resulting structures on the fly allows us to analyze thin film quality during the growth experiments.

The current work has demonstrated a complete crystallization pathway of $MAPbI_3$ perovskite with IPA antisolvent application, which has quickly initiated intermediate phase formation during spin-coating. The sample was subsequently annealed by an IR heater, and the resulting film showed the presence of mainly cubic $MAPbI_3$ perovskite and a tiny amount of PbI_2.

ACKNOWLEDGMENTS

This research is part of an infrastructure project funded by the German Federal Ministry for Science and Education (BMBF Project No. 05K19VTA).

We acknowledge the DESY (Hamburg, Germany) for the provision of experimental facilities. Parts of this research were carried out at PETRA III, and we would like to acknowledge Chen Shen and Rene Kirchhof for assistance using beamline P08. Beamtime was allocated for proposal I-20200254. We thank the LISA+ facility at Tübingen University for support.

AUTHOR DECLARATIONS

Conflict of Interest

The authors have no conflicts to disclose.

Author Contributions

Ekaterina Kneschaurek: Conceptualization (equal); Data curation (equal); Formal analysis (equal); Investigation (equal); Methodology (equal); Software (equal); Visualization (equal); Writing – original draft (equal); Writing – review & editing (equal). **Alexander Hinderhofer**: Conceptualization (lead); Funding acquisition (equal); Investigation (equal); Project administration (equal); Supervision (equal); Validation (equal); Writing – original draft (equal); Writing – review & editing (equal). **Bernd Hofferberth**: Conceptualization (equal); Investigation (equal); Methodology (lead); Resources (lead); Software (lead); Validation (equal). **Niels Schefczyk**: Data curation (equal); Investigation (equal); Methodology (equal); Validation (equal); Writing – review & editing (equal). **Linus Pithan**: Conceptualization (equal); Investigation (equal); Methodology (equal); Software (equal); Validation (equal); Writing – review & editing (equal). **Paul Zimmermann**: Investigation (equal); Methodology (equal); Software (equal); Validation

(equal); Writing – original draft (equal); Writing – review & editing (equal). **Lena Merten**: Investigation (equal); Methodology (equal); Validation (equal); Writing – review & editing (equal). **Florian Bertram**: Conceptualization (equal); Investigation (equal); Methodology (equal); Resources (equal); Software (equal); Writing – review & editing (equal). **Frank Schreiber**: Conceptualization (equal); Funding acquisition (equal); Methodology (equal); Project administration (equal); Resources (equal); Supervision (lead); Validation (equal); Writing – review & editing (equal).

DATA AVAILABILITY

The data that support the findings of this study are available from the corresponding author upon reasonable request.

REFERENCES

[1] B. Krause, F. Schreiber, H. Dosch, A. Pimpinelli, and O. H. Seeck, Europhys. Lett. **65**, 372–378 (2004).
[2] S. Kowarik, A. Gerlach, S. Sellner, F. Schreiber, L. Cavalcanti, and O. Konovalov, Phys. Rev. Lett. **96**, 125504 (2006).
[3] S. Kowarik, A. Gerlach, S. Sellner, F. Schreiber, J. Pflaum, L. Cavalcanti, and O. Konovalov, Phys. Chem. Chem. Phys. **8**, 1834–1836 (2006).
[4] N. E. Widjonarko, Coatings **6**, 54 (2016).
[5] H. Kohlmann, Z. Kristallogr. -Cryst. Mater. **232**, 843–849 (2017).
[6] H. Kohlmann, Eur. J. Inorg. Chem. **2019**, 4174–4180.
[7] L. A. Perez, K. W. Chou, J. A. Love, T. S. van der Poll, D.-M. Smilgies, T.-Q. Nguyen, E. J. Kramer, A. Amassian, and G. C. Bazan, Adv. Mater. **25**, 6380–6384 (2013).
[8] M. Abdelsamie, N. D. Treat, K. Zhao, C. McDowell, M. A. Burgers, R. Li, D.-M. Smilgies, N. Stingelin, G. C. Bazan, and A. Amassian, Adv. Mater. **27**, 7285–7292 (2015).
[9] D.-M. Smilgies, MRS Online Proc. Libr. **1695**, 14–18 (2014).
[10] P. Müller-Buschbaum, Adv. Mater. **26**, 7692–7709 (2014).
[11] K. A. Ritley, B. Krause, F. Schreiber, and H. Dosch, Rev. Sci. Instrum. **72**, 1453–1457 (2001).
[12] B. J. Norris, J. Anderson, J. F. Wager, and D. A. Keszler, J. Phys. D: Appl. Phys. **36**, L105–L107 (2003).
[13] T. Hosokai, A. Gerlach, A. Hinderhofer, C. Frank, G. Ligorio, U. Heinemeyer, A. Vorobiev, and F. Schreiber, Appl. Phys. Lett. **97**, 063301 (2010).
[14] C. Nicklin, T. Arnold, J. Rawle, and A. Warne, J. Synchrotron Radiat. **23**, 1245–1253 (2016).
[15] M. Scherzer, F. Girgsdies, E. Stotz, M.-G. Willinger, E. Frei, R. Schlögl, U. Pietsch, and T. Lunkenbein, J. Phys. Chem. C **123**, 13253–13262 (2019).
[16] K. Vegso, A. Shaji, M. Sojková, L. P. Slušná, T. Vojteková, J. Hrdá, Y. Halahovets, M. Hulman, M. Jergel, E. Majková, J. Wiesmann, and P. Šiffalovič, Rev. Sci. Instrum. **93**, 113909 (2022).
[17] *Physics of Organic Semiconductors*, 2nd ed., edited by W. Brütting and C. Adachi (John Wiley & Sons, Ltd., Hoboken, New Jersey, 2012), Vol. 2.
[18] J. Wagner, M. Gruber, A. Hinderhofer, A. Wilke, B. Bröker, J. Frisch, P. Amsalem, A. Vollmer, A. Opitz, N. Koch, F. Schreiber, and W. Brütting, Adv. Funct. Mater. **20**, 4295–4303 (2010).
[19] M. Kytka, A. Gerlach, F. Schreiber, and J. Kováč, Appl. Phys. Lett. **90**, 131911 (2007).
[20] U. Heinemeyer, K. Broch, A. Hinderhofer, M. Kytka, R. Scholz, A. Gerlach, and F. Schreiber, Phys. Rev. Lett. **104**, 257401 (2010).
[21] S. Bommel, N. Kleppmann, C. Weber, H. Spranger, P. Schäfer, J. Novak, S. V. Roth, F. Schreiber, S. H. L. Klapp, and S. Kowarik, Nat. Commun. **5**, 5388 (2014).
[22] K. T. Chaudhary, in *Thin Films*, edited by A. E. Ares (IntechOpen, Rijeka, 2021), Chap. 10.
[23] M. Jung, S.-G. Ji, G. Kim, and S. I. Seok, Chem. Soc. Rev. **48**, 2011–2038 (2019).
[24] M. A. Butt, Coatings **12**, 1115 (2022).
[25] H. Ogawa, T. Miyazaki, K. Shimokita, A. Fujiwara, M. Takenaka, T. Yamada, Y. Sugihara, and M. Takata, J. Appl. Crystallogr. **46**, 1610–1615 (2013).
[26] D. Barrit, A. D. Sheikh, R. Munir, J. M. Barbé, R. Li, D.-M. Smilgies, and A. Amassian, J. Mater. Res. **32**, 1899–1907 (2017).
[27] W.-R. Wu, C.-J. Su, W.-T. Chuang, Y.-C. Huang, P.-W. Yang, P.-C. Lin, C.-Y. Chen, T.-Y. Yang, A.-C. Su, K.-H. Wei, C.-M. Liu, and U.-S. Jeng, Adv. Energy Mater. **7**, 1601842 (2017).
[28] C. M. Sutter-Fella, Adv. Energy Mater. **11**, 2003534 (2021).
[29] H. Ogawa, M. Takenaka, T. Miyazaki, A. Fujiwara, B. Lee, K. Shimokita, E. Nishibori, and M. Takata, Macromolecules **49**, 3471–3477 (2016).
[30] D. T. W. Toolan, A. Isakova, R. Hodgkinson, N. Reeves-McLaren, O. S. Hammond, K. J. Edler, W. H. Briscoe, T. Arnold, T. Gough, P. D. Topham, and J. R. Howse, Macromolecules **49**, 4579–4586 (2016).
[31] K. Wei Chou, H. Ullah Khan, M. R. Niazi, B. Yan, R. Li, M. M. Payne, J. E. Anthony, D.-M. Smilgies, and A. Amassian, J. Mater. Chem. C **2**, 5681–5689 (2014).
[32] R. Fujimoto, Y. Yamashita, S. Kumagai, J. Tsurumi, A. Hinderhofer, K. Broch, F. Schreiber, S. Watanabe, and J. Takeya, J. Mater. Chem. C **5**, 12023–12030 (2017).
[33] M. Scheele, W. Brütting, and F. Schreiber, Phys. Chem. Chem. Phys. **17**, 97–111 (2015).
[34] I. A. Zaluzhnyy, R. P. Kurta, A. André, O. Y. Gorobtsov, M. Rose, P. Skopintsev, I. Besedin, A. V. Zozulya, M. Sprung, F. Schreiber, I. A. Vartanyants, and M. Scheele, Nano Lett. **17**, 3511–3517 (2017).
[35] A. Greco, A. Hinderhofer, M. I. Dar, N. Arora, J. Hagenlocher, A. Chumakov, M. Grätzel, and F. Schreiber, J. Phys. Chem. Lett. **9**, 6750–6754 (2018).
[36] N. Arora, A. Greco, S. Meloni, A. Hinderhofer, A. Mattoni, U. Rothlisberger, J. Hagenlocher, C. Caddeo, S. M. Zakeeruddin, F. Schreiber, M. Graetzel, R. H. Friend, and M. I. Dar, Commun. Mater. **3**, 2662 (2022).
[37] M. Qin, P. F. Chan, and X. Lu, Adv. Mater. **33**, 2105290 (2021).
[38] C.-Y. Chang, Y.-C. Huang, C.-S. Tsao, and W.-F. Su, ACS Appl. Mater. Interfaces **8**, 26712–26721 (2016).
[39] A. Brunova, K. Vegso, V. Nadazdy, P. Nadazdy, R. Subair, M. Jergel, E. Majkova, P. Pandit, S. V. Roth, A. Krasnansky, A. Hinderhofer, F. Schreiber, J. Tian, and P. Siffalovic, Adv. Mater. Interfaces **8**, 2100355 (2021).
[40] D. Barrit, M.-C. Tang, R. Munir, R. Li, K. Zhao, and D.-M. Smilgies, ACS Appl. Mater. Interfaces **14**, 26315–26326 (2022).
[41] P. Kovaricek, P. Nadazdy, E. Pluharova, A. Brunova, R. Subair, K. Vegso, V. L. P. Guerra, O. Volochanskyi, M. Kalbac, A. Krasnansky, P. Pandit, S. V. Roth, A. Hinderhofer, E. Majkova, M. Jergel, J. Tian, F. Schreiber, and P. Siffalovic, Adv. Funct. Mater. **31**, 2009007 (2021).
[42] V. Held, N. Mrkyvkova, P. Nádaždy, K. Vegso, A. Vlk, M. Ledinský, M. Jergel, A. Chumakov, S. V. Roth, F. Schreiber, and P. Siffalovic, J. Phys. Chem. Lett. **13**, 11905–11912 (2022).
[43] O. H. Seeck, C. Deiter, K. Pflaum, F. Bertam, A. Beerlink, H. Franz, J. Horbach, H. Schulte-Schrepping, B. M. Murphy, M. Greve, and O. Magnussen, J. Synchrotron Radiat. **19**, 30–38 (2011).
[44] B. Dou, V. L. Pool, M. F. Toney, and M. F. A. M. van Hest, Chem. Mater. **29**, 5931–5941 (2017).
[45] M. Qin, K. Tse, T.-K. Lau, Y. Li, C.-J. Su, G. Yang, J. Chen, J. Zhu, U.-S. Jeng, G. Li, H. Chen, and X. Lu, Adv. Mater. **31**, 1901284 (2019).
[46] R. Szostak, P. E. Marchezi, A. d. S. Marques, J. C. da Silva, M. S. de Holanda, M. M. Soares, H. C. N. Tolentino, and A. F. Nogueira, Sustainable Energy Fuels **3**, 2287 (2019).
[47] K. O. Brinkmann, J. He, F. Schubert, J. Malerczyk, C. Kreusel, F. van gen Hassend, S. Weber, J. Song, J. Qu, and T. Riedl, ACS Appl. Mater. Interfaces **11**, 40172–40179 (2019).
[48] R. Szostak, S. Sanchez, P. E. Marchezi, A. S. Marques, J. C. Silva, M. S. Holanda, A. Hagfeldt, H. C. N. Tolentino, and A. F. Nogueira, Adv. Funct. Mater. **31**, 2007473 (2021).
[49] Y. Yu, F. Zhang, T. Hou, X. Sun, H. Yu, and M. Zhang, Sol. RRL **5**, 2100386 (2021).